

## Promoting diesel soot combustion efficiency by tailoring the shapes and crystal facets of nanoscale $Mn_3O_4$

Fei Ji<sup>a</sup>, Yong Men<sup>a,\*</sup>, Jinguo Wang<sup>a</sup>, Yili Sun<sup>b</sup>, Zhendong Wang<sup>b</sup>, Biao Zhao<sup>a</sup>, Xiangtian Tao<sup>b</sup>, Guangjin Xu<sup>b</sup>

<sup>a</sup> College of Chemistry and Chemical Engineering, Shanghai University of Engineering Science, Shanghai, 201620, PR China

<sup>b</sup> SAIC Motor Commercial Vehicle Technical Center, Shanghai, 200438, PR China



### ARTICLE INFO

#### Keywords:

Nanoscale  $Mn_3O_4$   
Shape effect  
NO activation  
Surface oxygen species  
Diesel soot combustion

### ABSTRACT

Various shapes (hexagonal nanoplate, octahedral, and nanoparticle) of nanoscale  $Mn_3O_4$  have been successfully prepared via facile hydrothermal and co-precipitation methods, respectively, and evaluated for their performance on diesel soot combustion. The catalytic performance of hexagonal nanoplates  $Mn_3O_4$  ( $Mn_3O_4$ -HNS) is distinguished from the samples with other shapes by its superior activity on soot combustion with  $T_m$  of 407.7 °C and  $S_{CO_2}^m$  of 99.1% at the gas hourly space velocity of 9990  $h^{-1}$  with the feed composition of 2500 ppm NO/5 vol. %O<sub>2</sub>/N<sub>2</sub> under loose contact mode. The physicochemical properties of  $Mn_3O_4$  were systematically examined by different characterization techniques, including XRD, FTIR, BET, H<sub>2</sub>-TPR, FE-SEM, HR-TEM, XPS, soot-TPR, and NO/NO + O<sub>2</sub>-TPSR. The different crystal shapes controlled by the preparation method are found to influence the extent of exposed  $Mn_3O_4$  crystal facet, as determined by HR-TEM, which, in turn, was found to correlate with the catalytic performance. The kinetic study of soot combustion over these samples further revealed that the  $E_a$  obtained from three samples ranked as the order of (112) < (101) < (220) facets in reverse order of activity data, confirming the crystal-facet dependent reactivity. In view of the difference in catalytic activity and their physicochemical properties as estimated by various techniques, the superior catalytic performance of  $Mn_3O_4$ -HNS for diesel soot combustion was originated from its exposed (112) facet in association with its good lower temperature reducibility, abundant surface Mn<sup>4+</sup> and active oxygen species, and the enhanced NO oxidation capability. Furthermore, the best performing  $Mn_3O_4$ -HNS displayed the good stability through recycling test. Our work may provide an important insight on the design strategies to develop the high-efficient soot combustion catalysts under the working conditions of the diesel engines.

### 1. Introduction

Over the past few decades, diesel engines with direct fuel injection have become as a major power source for vehicles, ships, locomotives and heavy-duty machines due to their optimal fuel efficiency, high durability and low cost compared to gasoline filled engines with a similar power [1,2]. However, particulate matters (PM) along with nitrogen oxides (NO<sub>x</sub>) and unburned hydrocarbons in the exhaust emitted from the diesel engines are considered to be substantial contributors seriously jeopardizing human's health and environment [3–6]. Particularly, soot particulates, as one of the major pollutants, can have detrimental impact on human respiratory system hazards by penetrating into the lung cells such as asthma, bronchitis, lung cancer, and cardiovascular and allergic diseases [7–9]. Therefore, the elimination of soot particulates is of great significance to the modern society.

Consequently, to reduce soot particulates emissions below the limits imposed by the regulations standards, the diesel particulate filters (DPFs) is regarded as an economical and efficient after-treatment technology for the collection of the maximum possible amount of diesel soot particulates among various technologies [10].

The exhaust from diesel engine is normally in the temperature range of 200 ~ 500 °C, but the DPFs need periodically regenerate the plugged soot filtration at high temperature above 600 °C [11] to reduce DPFs backpressure and contain the high fuel efficiency. Therefore, the development of the efficient soot combustion catalyst which can burn soot particles at the low ignition temperature ( $T_{ig}$ ) and has high thermal stability, is highly desirable to be further integrated with the self-generable soot particulate filter (SSF) [12].

So far, two key challenges are needed to be addressed for improving the catalytic efficiency: one is to design catalysts with rational structure

\* Corresponding author.

E-mail address: [men@sues.edu.cn](mailto:men@sues.edu.cn) (Y. Men).

to enlarge the contact area between soot and catalyst [13–16], the other is to develop catalysts with excellent intrinsic reactivity [17–19]. In the effort to develop highly active catalysts, noble metal have been extensively investigated as the major components of oxidation catalysts used for soot combustion in the presence of NO, for instance, 3DOM Au@Pt/CZO [20], 3DOM Au<sub>n</sub>/LaFeO<sub>3</sub> [12], Pt<sub>3</sub>Sn/CeO<sub>2</sub> [8], Ag/PrMnO<sub>3+δ</sub> [21], and Pt/Ce50Pr50-NP [22]. Despite their great activity for soot combustion, the major obstacle in implementing noble metal for soot combustion is the cost associated with current catalyst formulations, which limits the economic viability and impedes their widespread use in soot combustion to niche applications. Hence, to meet the actual catalytic environment and emission standards of particulate matters, the design and development of novel highly efficient and inexpensive nanocatalysts was still the primary challenge.

Extensive studies over the past several decades have verified that nanoscale metal oxides with special structure and shape profoundly tuned the catalytic chemical reaction performance and selectivity [13,14,23–25]. Lately, more and more attention has been focused on synthesize soot combustion catalysts with designed special morphology to increase the intrinsic reactivity [17–19]. Trovarelli et al. [18] reported that soot combustion activity is strongly dependent on the shape of the ceria nanoparticles, and the exposed (100) surface facets were considered to facilitate soot combustion. Manganese-based oxides such as MnO<sub>2</sub>, Mn<sub>2</sub>O<sub>3</sub>, and Mn<sub>3</sub>O<sub>4</sub> with different crystal types (α, β, γ, or δ), being prospective candidate materials, were widely applied as efficient catalysts for the removal of volatile organic compounds (VOCs) and diesel exhaust in the literatures [9,26–32]. The outstanding performance of manganese oxide catalysts is mainly attributed by enhanced redox properties and the facile redox cycle of Mn<sup>2+</sup>/Mn<sup>3+</sup> or Mn<sup>3+</sup>/Mn<sup>4+</sup> associated with the multi-valence Mn<sup>δ+</sup> species on the catalysts surface. Significant efforts have been recently made to develop efficient manganese oxides combustion catalysts with unique morphologies and structures. Li et al. [27] investigated low-temperature oxidation of ethanol over 1D-MnO<sub>2</sub>, 2D-MnO<sub>2</sub> and 3D-MnO<sub>2</sub>, and the superior performance of 3D-MnO<sub>2</sub> was interpreted by the enhanced low temperature reducibility and more abundant surface adsorbed oxygen species and Mn<sup>4+</sup> ions compared to 1D-MnO<sub>2</sub> and 2D-MnO<sub>2</sub>. Zhan et al. [30] studied that the degradation of methylene blue (MB) over size and shape-controlled Mn<sub>3</sub>O<sub>4</sub> nanocrystals, and found that octahedral Mn<sub>3</sub>O<sub>4</sub> nanostructures exhibited a capacity for very high (above 99.7%) degradation of MB, which was mainly caused by the synergistic effect of octahedral Mn<sub>3</sub>O<sub>4</sub> with exposed the facet of (111) and H<sub>2</sub>O<sub>2</sub>. More recently, we reported crystal facet-dependent reactivity of α-Mn<sub>2</sub>O<sub>3</sub> microcrystalline catalyst for soot combustion [17], and the enhanced reactivity was originated from chemical nature of the exposed (001) crystal facets, on which the higher concentration of low-coordinated surface oxygen sites facilitates the oxygen activation and improves surface redox properties, thereby accelerating the formation of the crucial intermediate i.e. NO<sub>2</sub> formation by NO oxidation and thus promoting the overall soot combustion efficiency.

Although the considerable advances have been achieved to develop inexpensive Mn-based soot combustion catalysts, there is still much to be explored to deepen our understanding on the structure-activity relationship by tuning the shapes and exposed crystal facet of Mn<sub>3</sub>O<sub>4</sub>. To the best of our knowledge, this is the first investigation targeting at using the nanoscale Mn<sub>3</sub>O<sub>4</sub> with different shapes and exposed crystal facets for soot combustion. In this work, we report the controllable synthesis of Mn<sub>3</sub>O<sub>4</sub> in the form of hexagonal nanoplate, octahedral nanocrystal, and nanoparticle and their catalytic performance for soot combustion. Moreover, the physicochemical properties of the synthesized nanoscale Mn<sub>3</sub>O<sub>4</sub> catalysts were systematically examined by means of different characterization techniques, including XRD, FTIR, BET, H<sub>2</sub>-TPR, FE-SEM, HR-TEM, XPS, soot-TPR, and NO/NO + O<sub>2</sub>-TPSR. Our results revealed that hexagonal nanoplates Mn<sub>3</sub>O<sub>4</sub> catalyst exhibited remarkably enhanced catalytic activity as compared with Mn<sub>3</sub>O<sub>4</sub> in octahedral and nanoparticle, which is corroborated with the

characterization and kinetic results.

## 2. Experimental section

### 2.1. Preparation of Mn<sub>3</sub>O<sub>4</sub> nanocrystals

#### 2.1.1. Materials

All the chemicals were purchased from commercial suppliers and used as received without further purification.

**2.1.1.1. Synthesis of Mn<sub>3</sub>O<sub>4</sub> hexagonal nanoplates.** For a typical procedure, MnAc<sub>2</sub> aqueous solution (0.2 M, 30 mL) was added dropwise to NaOH (2 M, 30 mL) under continuous stirring for 30 min. After that, glucose (1.0089 g, 5.6 mmol) was dissolved to the above solution under stirring another 20 min at room temperature. Then, the mixture liquid was transferred into a 100 mL Teflon-lined stainless steel autoclave and heated at 180 °C for 21 h. After hydrothermal procedure, the autoclave was cooled down to room temperature naturally. The as-prepared brown precipitate precursor was obtained by centrifugation, washed thoroughly for three times with distilled water and absolute ethanol to remove any impurities, and then subsequently dried at 80 °C overnight in an oven. Finally, the precursor was calcined at 500 °C for 3 h with a ramp rate of 5 °C/min in air flow, and the resulting sample was marked as Mn<sub>3</sub>O<sub>4</sub>-HNS.

**2.1.1.2. Synthesis of Mn<sub>3</sub>O<sub>4</sub> octahedral nanocrystals.** In a typical synthesis, the Na<sub>2</sub>B<sub>4</sub>O<sub>7</sub> aqueous solution (0.2 M, 20 mL) was added dropwise into the MnAc<sub>2</sub> solution (0.2 M, 20 mL) under stirring at room temperature to form a white homogeneous liquid. After that, NaOH (40 mmol) was added quickly to the above solution, and then the resulting reaction mixture turned to brown turbid liquid, which was stirred for about 24 h at room temperature. After the reaction was completed, the resulting as-synthesized brown solid product was filtered and washed for three times with distilled water and absolute ethanol to remove ions, and dried in vacuum oven at 40 °C for 6 h. The dried sample was calcined at 500 °C in air for 2 h to yield the Mn<sub>3</sub>O<sub>4</sub> octahedral nanocrystals, which was marked as Mn<sub>3</sub>O<sub>4</sub>-ONS.

**2.1.1.3. Synthesis of Mn<sub>3</sub>O<sub>4</sub> nanoparticles.** Mn(NO<sub>3</sub>)<sub>2</sub> aqueous solution (50%, 5.7264 g) was added dropwise into the NaOH solution (1 M, 60 mL) under stirring for 10 min, which was then transferred into a Teflon-lined stainless steel autoclave of 100 mL capacity, sealed and maintained at 160 °C for 18 h in an oven. The resulting precipitate was collected by centrifugation, and then washed with deionized water and ethanol. The material was dried at 80 °C overnight and calcined at 500 °C for 2 h under air flow to obtain Mn<sub>3</sub>O<sub>4</sub> nanoparticles, which was marked as Mn<sub>3</sub>O<sub>4</sub>-NPS.

### 2.2. Materials characterization

The power X-ray diffraction (XRD) patterns were recorded on a Bruker: D2 Phaser system, using Cu K $\alpha$  radiation combined with nickel filter operating at  $\lambda = 1.54056 \text{ \AA}$ , 30 kV and 10 mA from 15–80° (20 values) and the scan speed during analysis was 0.5 s/step. The obtained patterns were analyzed by using Jade software for phase identification. The average crystallite sizes (D) of catalysts were determined by the Scherrer equation ( $D = K\lambda/(\beta \cdot \cos \theta)$ ). The Fourier transform infrared (FTIR) spectra of the catalyst were collected by using a Nicolet 380 spectrometer in the range of 400–4000 cm<sup>−1</sup>. The N<sub>2</sub> adsorption-desorption isotherms, structural parameter and pore size distribution were obtained by using the Brunauer-Emmet-Teller (BET) and Barrett-Joyner-Halenda (BJH) models on a Micromeritics ASAP 2460 analyzer at liquid nitrogen temperature (77 K). The samples were degassed at 100 °C for 5 h in flowing N<sub>2</sub> before testing. The field emission-scanning electron microscopy (FE-SEM) images were taken on Hitachi S-4800 apparatus. High-resolution transmission electron microscopy (HR-TEM)

images of the catalysts were taken on Hitachi JMF-2100 instrument. The X-ray photoelectron spectroscopy (XPS) measurements of the synthesized samples were analyzed on ESCALAB 250 Xi with Al-K $\alpha$  X-ray source. And the narrow scan spectra of Mn 2p, Mn 3s and O 1s were recorded in the binding energy range from 0 to 900 eV by using pass energy of 40 eV. C 1s signal from adventitious hydrocarbon at 284.6 eV was used as an energy reference to correct for charging. All XPS spectra were carried out using XPS peak software package.

### 2.3. Temperature-programmed reduction (TPR), and temperature-programmed surface reaction (TPSR)

The hydrogen temperature-programmed reduction (H<sub>2</sub>-TPR) was carried out on a chemisorption analyzer (Micromeritics, Auto Chem II2920) instrument. 50 mg of the catalyst (40–60 mesh) was pretreated in Ar flow of 50 mL/min for 1 h at 200 °C in a U-shaped fixed-bed quartz micro-reactor, and then cooled down to 100 °C. After the pretreatment, the catalyst was reduced in a flow (30 mL/min) of 10 vol.% H<sub>2</sub>/Ar in the temperature range of 100 °C–900 °C with a heating rate of 10 °C/min. H<sub>2</sub> consumption was recorded by using a thermal conductivity detector (TCD), which was calibrated by the reduction of known amounts of Ag<sub>2</sub>O. The soot temperature-programmed reduction (soot-TPR) was tested in a fixed-bed tubular quartz system. The soot-catalyst mixture (110 mg, the catalyst-to-soot mass ratio of 10) under loose contact mode was pretreated at 200 °C for 30 min in the He atmosphere (80 mL/min) to remove surface carbonates and/or chemisorbed CO<sub>2</sub> existed on the Mn<sub>3</sub>O<sub>4</sub> samples, and then heated up to 800 °C at a heating rate of 2 °C/min in He. The effluent gases were detected by an online mass spectrometer and the mass number (*m/z*) of 44 and 28 were used for monitoring CO<sub>2</sub> and CO, respectively.

The temperature-programmed surface reaction in the presence of NO with O<sub>2</sub> (NO + O<sub>2</sub>-TPSR) or without O<sub>2</sub> (NO-TPSR) on the different catalysts were carried out on a fixed-bed tubular quartz system. The reaction products were detected by an online mass spectrometer (Hiden, HPR-20). 50 mg of catalyst previously treated at 500 °C with 40 mL/min of 10 vol.% O<sub>2</sub>/He for 1 h, and then cooled to 100 °C. The NO + O<sub>2</sub>-TPSR experiment were performed with 5000 ppm NO-5 vol.% O<sub>2</sub> balanced with He flow of 40 mL/min by ramping reaction temperature from 100 °C to 700 °C at a heating rate of 5 °C/min. In the NO-TPSR measurement, the reactant gases were replaced by 1 vol.% NO balanced with He.

### 2.4. Catalyst performance evaluation

The catalytic soot combustion efficiency over a series of Mn<sub>3</sub>O<sub>4</sub> catalysts with the same mass basis were studied at atmospheric pressure by a temperature programmed oxidation (TPO) reaction in a fixed-bed reactor ( $\Phi = 6.0$  mm), which was equipped with a K-type thermocouple in the center of the tube furnace to accurately measure the temperature of the soot/catalyst bed (see Fig. S1). The catalyst and soot (10 mg) (MA100 Mitsubishi, Japan) mixture (10:1, catalyst/soot weight ratio) was mixed carefully for five minutes by using a spatula to reproduce the loose contact conditions, which could perform the test under the conditions as much as close to the real practical conditions. Prior to each catalytic test, the catalyst and soot were pre-treated at 200 °C for 30 min under nitrogen of 80 mL/min for 30 min. After the pre-treatment, the total feed gases flow rate was adjusted to be 80 mL/min including 2500 ppm NO and 5 vol.% O<sub>2</sub> balanced by N<sub>2</sub>, thus giving a gas hourly space velocity (GHSV) of 9990 h<sup>-1</sup>. The reaction temperature was increased from 200 °C to 700 °C at a heating rate of 2 °C/min. The concentrations of CO<sub>2</sub> and CO in the effluent gases were determined using an on-line automobile emission analyzer (HPC 500). Four activity test cycles were carried out for each sample under the same atmospheres to examine the stability of the catalysts. A blank experiment was carried out in the absence of catalyst under the aforementioned experimental conditions. The effect of water vapor in the feed gases on the

combustion efficiencies of soot was also evaluated under condition of 10 vol.% H<sub>2</sub>O, which was carried by a syringe pump. To study the effect of contact mode Mn<sub>3</sub>O<sub>4</sub> samples and soot particles, the sample and soot mixture was smoothly grounded in an agate mortar to simulate the test for tight contact mode. The Mn<sub>3</sub>O<sub>4</sub> sample was aged under the atmosphere of 10 vol.% H<sub>2</sub>O/10 vol.% O<sub>2</sub>/N<sub>2</sub> at 850 °C for 4 h and the accelerated deactivation test of catalyst was evaluated under loose contact mode. The catalytic soot combustion efficiency were evaluated and compared in terms of T<sub>m</sub> (the temperature which has the maximum concentration of CO<sub>2</sub>) and S<sub>CO2</sub> (CO<sub>2</sub> selectivity), which was calculated from the CO<sub>2</sub> content as follows the Eq. (1):

$$S_{CO2} = \frac{[CO2]}{[CO] + [CO2]} * 100\% \quad (1)$$

In this equation, [CO<sub>2</sub>] means the CO<sub>2</sub> outlet molar concentration; [CO] means the CO outlet molar concentration. S<sub>CO2</sub><sup>m</sup> was defined as the S<sub>CO2</sub> at T<sub>m</sub>.

### 2.5. Kinetic study in soot combustion

To obtain the activation energy (E<sub>a</sub>) of the samples, the kinetic studies were carried out under similar feed gas compositions, containing 0.25 vol.% NO-5 vol.% O<sub>2</sub> and N<sub>2</sub> as the equilibrium gas, but the GHSV increased to twice of 9990 h<sup>-1</sup>. To ensure the samples works in the kinetic region, the kinetic values was calculated using soot conversion rates below 12% according to the Eq. (2):

$$\ln R = -A \exp\left(-\frac{E_a}{RT}\right) \quad (2)$$

Here, R and T were the soot reaction rate (mol·min<sup>-1</sup> m<sup>-2</sup>) and reaction temperature (K), respectively.

## 3. Results and discussion

### 3.1. Crystal structures and morphologies of catalysts

Fig. 1 showed the very similar XRD patterns of Mn<sub>3</sub>O<sub>4</sub>-HNS, Mn<sub>3</sub>O<sub>4</sub>-ONS, and Mn<sub>3</sub>O<sub>4</sub>-NPS samples. The diffraction peaks located at 17.9°, 29°, 32.4°, 36.1°, 44.5°, 50.9°, 58.5°, 59.8°, and 64.6° corresponded to the (101), (112), (103), (211), (220), (105), (321), (224), and (440) planes, respectively. These peaks could be readily indexed to a pure phase of Mn<sub>3</sub>O<sub>4</sub> (tetragonal hausmannite spinel structure, I41/amd) with the lattice constants a = 0.5762, c = 0.9469 nm, and Z = 4, in consistence with the values previous reported for bulk Mn<sub>3</sub>O<sub>4</sub> (JCPDS No.24-0734) [33]. No diffraction peaks of any other impurity phases were detected in this XRD studies, indicating high purity of the synthesized Mn<sub>3</sub>O<sub>4</sub> materials. Table 1 shows the calculated crystallite sizes

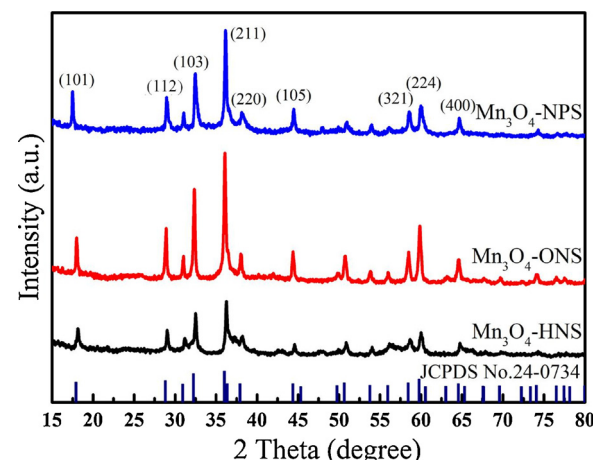


Fig. 1. XRD patterns of Mn<sub>3</sub>O<sub>4</sub>-HNS, Mn<sub>3</sub>O<sub>4</sub>-ONS, and Mn<sub>3</sub>O<sub>4</sub>-NPS.

**Table 1**

Surface fraction of exposed (112), (101), and (220) facets, preparation parameters, crystallite size, BET specific surface area ( $S_{BET}$ ), pore volume ( $V_p$ ), pore diameter ( $D_p$ ), the ratio of  $Mn^{4+}/Mn^{2+}$  and specific reaction rates ( $R_s$ ) for the three  $Mn_3O_4$  samples.

Samples	(112) [%] <sup>a</sup>	(101) [%] <sup>a</sup>	(220) [%] <sup>a</sup>	Crystallite size <sup>b</sup> (nm)	$S_{BET}$ <sup>c</sup> (m <sup>2</sup> /g)	$V_p$ (cm <sup>3</sup> /g)	$D_p$ <sup>d</sup> (nm)	The ratio <sup>e</sup> of $Mn^{4+}/Mn^{2+}$	$R_s$ <sup>f</sup> (μmol·s <sup>-1</sup> m <sup>-2</sup> )
$Mn_3O_4$ -HNS	68.4	31.6	0	26.3	18.6	0.091	21.1	0.88	5.13
$Mn_3O_4$ -ONS	0	100.0	0	35.6	28.5	0.206	29.5	0.74	1.02
$Mn_3O_4$ -NPS	0	82.0	18.0	38.0	8.6	0.053	25.1	0.67	0.27

<sup>a</sup> Area percentage of (112), (101), and (220) facets were estimated based on FE-SEM/HR-TEM images (about 50 nanoparticles were used for averaging).

<sup>b</sup> The crystallite sizes based on (101), (112) and (220) diffraction peaks were calculated by the Scherrer equation ( $D = K\lambda / (\beta \cos \theta)$ ).

<sup>c</sup> Specific surface areas were calculated by the BET method.

<sup>d</sup> The data was calculated via the BJH method according to the  $N_2$  desorption isotherms.

<sup>e</sup> The ratio were calculated based on the peak areas processed by the XPS-Peak software.

<sup>f</sup>  $R_s$  were calculated based on the weight of the catalysts of 0.1 g,  $P = 101.3$  kPa,  $T = 320$  °C under loose contact mode, and the feed composition: 2500 ppm NO, 5 vol.% O<sub>2</sub> and balanced by N<sub>2</sub> with the total flow of 80 mL/min.

of  $Mn_3O_4$  based on (101), (112) and (220) XRD diffraction peaks were 26.3, 35.6 and 38.0 nm for  $Mn_3O_4$ -HNS,  $Mn_3O_4$ -ONS and  $Mn_3O_4$ -NPS, respectively. FTIR spectra in Fig. S2 showed that three  $Mn_3O_4$  samples exhibited similar absorption peaks in the range of 400–4000 cm<sup>-1</sup>, agreeing well with the previous results reported in the literatures [34]. Two peaks at 629 and 528 cm<sup>-1</sup> were attributable to the Mn-O band stretching modes of tetrahedral and distortion vibration in an octahedral environment, respectively. The absorption peak at 413 cm<sup>-1</sup> corresponded to the Mn-O vibration in octahedral sites in  $Mn_3O_4$ . The peak observed at 2353 cm<sup>-1</sup> was assigned to the carbon dioxide. The broad absorption bands centered at 1625 and 3439 cm<sup>-1</sup> could be related to the bending vibration of hydroxyl combined with Mn atoms and the O-H stretching vibrations of absorbed water molecules from the atmosphere, respectively. These FTIR observations confirmed that no additional/impurity phase was formed which further supports our XRD and XPS results.

Fig. 2 displays the surface morphologies of the  $Mn_3O_4$  catalysts analyzed by FE-SEM. As depicted in Fig. 2a, one can see that  $Mn_3O_4$ -HNS had an integrated hexagonal nanoplate morphology with a diameter of 80–150 nm. In Fig. 2b,  $Mn_3O_4$ -ONS presented octahedral morphology with the size ranging from 60 to 120 nm. It was observed in Fig. 2c that  $Mn_3O_4$ -NPS samples possessed irregular spherical morphology with the nanoparticle size of about 100 nm. The three types of  $Mn_3O_4$  samples presented slight agglomeration phenomena, likely due to their small nanoparticle size in the range < 150 nm.

HR-TEM is a very useful tool to identify the lattice spacing and exposed crystallite facets on the catalysts surface. The structure and morphology of the  $Mn_3O_4$  catalysts were examined by HR-TEM in details and shown in Fig. 3. It was noted that the size of  $Mn_3O_4$ -HNS with hexagonal nanoplate shapes (in Fig. 3a and b) is in the range from 60 to 120 nm while the hexagonal nanoplate with an interplanar distance of 0.492 nm and 0.309 nm corresponding to (101) and (112) crystal facet of hausmannite  $Mn_3O_4$  (Fig. 3c). Notably,  $Mn_3O_4$ -ONS sample in a low-magnification image of Fig. 3d showed a perfect octahedral nanocrystallite in the size ranging from 60 to 120 nm. The HR-TEM (Fig. 3f) images showed the lattice fringes at 0.492 nm, corresponding a clear crystallite growth along the [101] crystallographic direction. From

Fig. 3g and h, the  $Mn_3O_4$ -NPS nanocrystallites were visible as nanoparticles mostly in the range 90–100 nm, over which (101) and (220) facets were identified by the lattice fringe spacing of 0.492 nm and 0.204 nm, respectively. The HR-TEM results validate that  $Mn_3O_4$ -ONS exclusively exposed (101) facets, whereas the  $Mn_3O_4$ -HNS and  $Mn_3O_4$ -NPS co-exposed (112)/(101) and (101)/(220) facets, respectively. The results of HR-TEM were consistent with the FE-SEM, which were also in good agreement with the previous reports [28,32,35,36].

The fraction of each exposed crystal facet estimated according to the geometric models based on 50 nanoparticles in the FE-SEM and HR-TEM observations were summarized in Table 1. Based on the values of exposed (101), (112), and (220) facets, the overall catalytic activity of three types of nanoscale  $Mn_3O_4$  samples followed the order of the exposure fraction in the following exposed crystal facets: (112) > (101) > (220).

### 3.2. Surface area and chemical properties

In Fig. S3A, all  $N_2$  adsorption-desorption isotherms from the samples exhibited the type IV with H3 hysteresis loops at relatively high pressure ( $P/P_0$ : 0.6–1.0), indicating that these samples exhibited typical characteristic of mesoporous materials. The BJH pore size distribution for  $Mn_3O_4$  samples derived from the  $N_2$  adsorption-desorption isotherms indicated that all  $Mn_3O_4$  samples displayed a broad mesoporous distribution at 20–40 nm (Fig. S3B). Table 1 summarized the detailed physical parameters of all three samples. The BET surface areas of  $Mn_3O_4$ -HNS,  $Mn_3O_4$ -ONS, and  $Mn_3O_4$ -NPS were determined to be 18.6, 28.5, and 8.6 m<sup>2</sup>/g, respectively.

$H_2$ -TPR measurements were employed to investigate the reducibility of Mn-based oxides. The  $H_2$ -TPR curves of  $Mn_3O_4$  exhibited two typical reduction peaks between 150 and 500 °C in Fig. 4, which can be attributed to the stepwise reduction of  $Mn^{4+} \rightarrow Mn^{3+} \rightarrow Mn^{2+}$  under  $H_2$  atmosphere. The  $Mn_3O_4$ -HNS sample showed a broad peak with a maximum at 323.7 °C and a low temperature shoulder reduction peak at 285.3 °C. The  $Mn_3O_4$ -ONS and  $Mn_3O_4$ -NPS both presented two well-resolved peaks, showing the low-temperature peak at 286.5 and 316.2 °C, and the high-temperature peak at 402.7 and 411.1 °C,

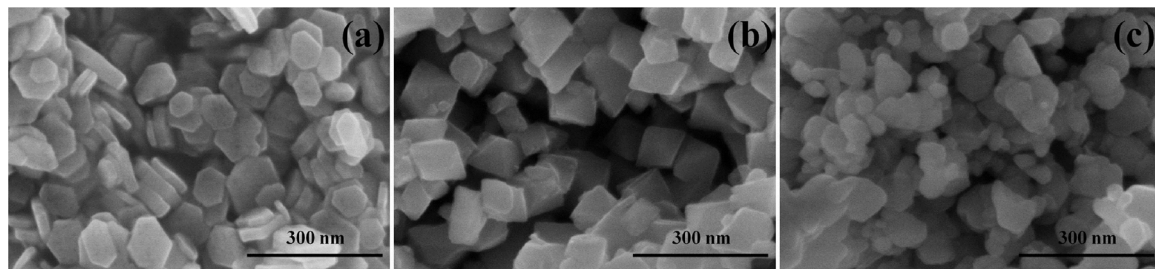


Fig. 2. FE-SEM images of three  $Mn_3O_4$  samples,  $Mn_3O_4$ -HNS (a),  $Mn_3O_4$ -ONS (b), and  $Mn_3O_4$ -NPS (c).

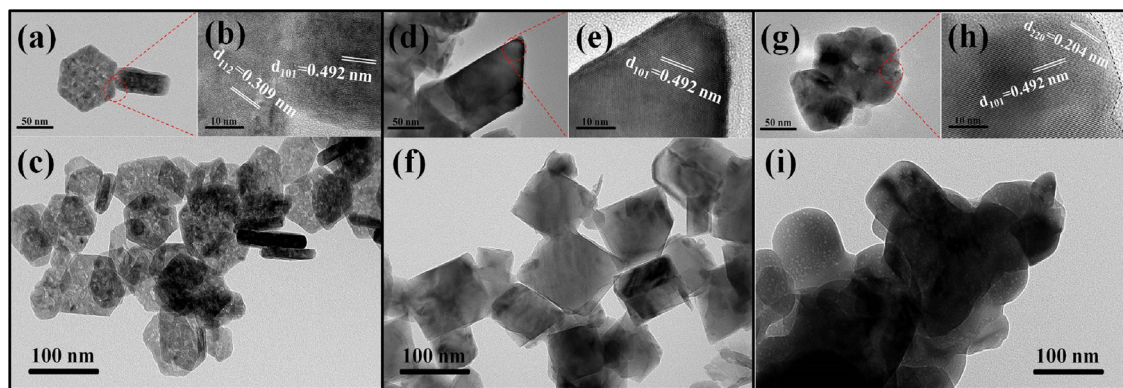


Fig. 3. HR-TEM images of three  $\text{Mn}_3\text{O}_4$  samples,  $\text{Mn}_3\text{O}_4$ -HNS (a,b,c),  $\text{Mn}_3\text{O}_4$ -ONS (d,e,f), and  $\text{Mn}_3\text{O}_4$ -NPS (g,h,i).

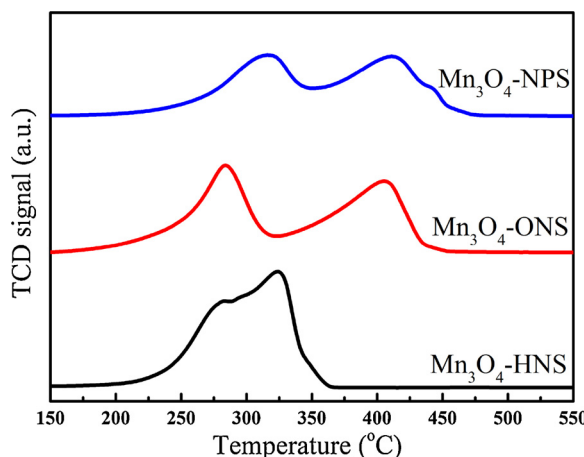


Fig. 4.  $\text{H}_2$ -TPR curves for three  $\text{Mn}_3\text{O}_4$  samples.

respectively. The reduction peak of  $\text{Mn}_3\text{O}_4$ -HNS shifted towards much lower temperature compared with that of the  $\text{Mn}_3\text{O}_4$ -ONS and  $\text{Mn}_3\text{O}_4$ -NPS samples. The low-temperature peak can be ascribed to the reduction of  $\text{Mn}^{4+}$  ion species of  $\text{Mn}_3\text{O}_4$  sample to  $\text{Mn}^{3+}$ . The two low temperature peaks of  $\text{Mn}_3\text{O}_4$ -HNS sample can be attributed to the reduction of the respective  $\text{Mn}^{4+}$  species in associated with the exposed (112) and (101) crystal facets. The origin of the different reducibility of  $\text{Mn}^{4+}$  species may be closely related to their shape-dependent redox properties of  $\text{Mn}_3\text{O}_4$  catalysts. The reduction degree and the  $\text{H}_2$  consumption were quantified based on the  $\text{H}_2$ -TPR profiles and summarized in Table 2. The  $\text{H}_2$  consumption for low-temperature peak decreased with the order of  $3.1 \text{ mmol/g}$  for  $\text{Mn}_3\text{O}_4$ -HNS  $> 2.9 \text{ mmol/g}$  for  $\text{Mn}_3\text{O}_4$ -ONS  $> 2.5 \text{ mmol/g}$  for  $\text{Mn}_3\text{O}_4$ -NPS. And the  $\text{H}_2$  uptake for high-temperature peak followed the same order of  $2.8 \text{ mmol/g}$  for  $\text{Mn}_3\text{O}_4$ -HNS  $\cong 2.8 \text{ mmol/g}$  for  $\text{Mn}_3\text{O}_4$ -ONS  $> 2.6 \text{ mmol/g}$  for  $\text{Mn}_3\text{O}_4$ -NPS. It is generally accepted in the literatures that the shape of manganese oxides catalysts determined the chemical properties and catalytic performance

by affecting their exposed crystal facets [17,27,37]. In this study, the different exposed crystal facets and surface structure led to the differences in the content of surface  $\text{Mn}^{4+}$  and surface oxygen species on (112), (101) and (220) crystal facets, and consequently determined their catalytic behaviors for soot combustion. Based on the previous fundamental studies on the relationship of surface structure and catalytic activity [37–39], the catalysts with exposed high-index planes such as (112) and (211) surfaces generally exhibited much higher catalytic activity than those having low-index planes such as (111), (101), and (110) surfaces, since high-index surfaces have a higher density of unsaturated atomic steps, edges, corners and kinks, which can serve as active sites for breaking chemical bonds. Comparing the peak positions of three different as-synthesized catalysts, the high reducibility of the  $\text{Mn}_3\text{O}_4$ -HNS is originated from the more open surface structure and the increased fraction of exposed (112) facets with abundant  $\text{Mn}^{4+}$  ions and surface active oxygen species. According to  $\text{H}_2$ -TPR results, it is concluded that  $\text{Mn}_3\text{O}_4$ -HNS sample possessed the largest amount of surface  $\text{Mn}^{4+}$  species over co-exposed (112) and (101) crystal facets, and thereby performed the best low-temperature reducibility.

The oxidation state of Mn ions and chemical composition in the synthesized  $\text{Mn}_3\text{O}_4$  samples were analyzed using X-ray photoelectron spectroscopy (XPS). The XPS survey spectra of all  $\text{Mn}_3\text{O}_4$  samples in Fig. S4 provided the evidence for the presence of C, O and Mn elements over different  $\text{Mn}_3\text{O}_4$  samples. No other extra/impurity elements peaks were identified in this XPS patterns, implying the purity of the synthesized samples which was further confirmed from XRD studies.

The regional scan of Mn 2p, O 1s and Mn 3s peaks were presented in Fig. 5. As seen from Fig. 5A, the spectrum of Mn 2p presented spin-orbit splitting into  $2p_{1/2}$  and  $2p_{3/2}$  components, corresponding to the different binding energy (BE) of 652.9 eV and 641.5 eV with energy splitting of 11.4 eV. Obviously, three components of Mn 2p<sub>3/2</sub> peak with BE of 640.7, 641.7 and 642.6 eV can be observed, which were assigned to  $\text{Mn}^{2+}$ ,  $\text{Mn}^{3+}$  and  $\text{Mn}^{4+}$  cations, respectively [40]. Based on the XPS analysis, the surface elemental composition, chemical state and quantitative results have been summarized and listed in Table 2. It can be seen that the  $\text{Mn}^{4+} / (\text{Mn}^{3+} + \text{Mn}^{2+})$  ratio of all the catalysts

Table 2

$\text{H}_2$  consumptions, surface element composition, catalytic activity, and the  $E_a$  values of three  $\text{Mn}_3\text{O}_4$  samples.

Samples	Reduction temperature (°C)		$\text{H}_2$ consumption (mmol/g)			Surface element molar ratio <sup>a</sup>	$T_m$ <sup>b</sup> (°C)	$S_{\text{CO}_2}$ <sup>b</sup> (%)	$E^b$ (kJ/mol)	
	Peak 1	Peak 2	$\text{Mn}^{4+} \rightarrow \text{Mn}^{3+}$	$\text{Mn}^{3+} \rightarrow \text{Mn}^{2+}$	Total					
$\text{Mn}_3\text{O}_4$ -HNS	285.3	323.7	3.1	2.8	5.9	0.75	0.59	407.7	99.1	56.4
$\text{Mn}_3\text{O}_4$ -ONS	286.5	402.7	2.9	2.8	5.7	0.60	0.42	427.8	96.7	86.4
$\text{Mn}_3\text{O}_4$ -NPS	316.2	411.1	2.5	2.6	5.1	0.53	0.39	454.6	96.5	100.6

<sup>a</sup> The ratios were calculated based on the peak areas processed by the XPS-Peak software.

<sup>b</sup> The values were calculated based on the weight of the catalysts of 0.1 g under loose contact mode, and the feed composition: 2500 ppm NO, 5 vol.%  $\text{O}_2$  and balanced by  $\text{N}_2$  with the total flow of 80 mL/min.

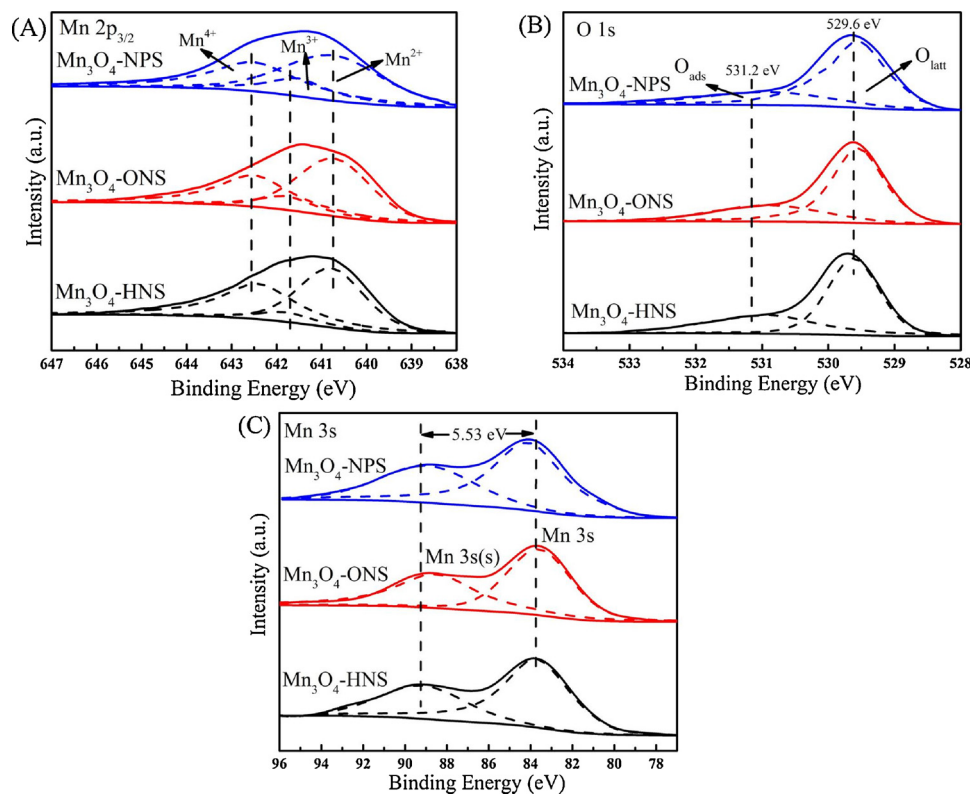


**Fig. 5.** XPS spectra of (A) Mn 2p<sub>3/2</sub>, (B) O 1 s, and (C) Mn 3 s for three Mn<sub>3</sub>O<sub>4</sub> samples. The solid line was the experimental data, and the dash line was the peak fitting data.

increased in the order of Mn<sub>3</sub>O<sub>4</sub>-NPS (0.53) < Mn<sub>3</sub>O<sub>4</sub>-ONS (0.60) < Mn<sub>3</sub>O<sub>4</sub>-HNS (0.75), implying that the (112) facets contained more Mn<sup>4+</sup> cations than that of (101) facets. According to the literatures [27,41], some experimental and theoretical studies have pointed out that the Mn<sup>4+</sup> cations are the much more reactive sites for the oxidation reactions, and as a result the abundant Mn<sup>4+</sup> cations on the catalyst surface could facilitate soot combustion efficiency. Therefore, the chemical state of Mn could be one of the important influencing factors for promoting catalytic performances of the Mn<sub>3</sub>O<sub>4</sub> samples.

O 1 s XPS spectra in Fig. 5B demonstrated two fitted oxygen peaks for three Mn<sub>3</sub>O<sub>4</sub> samples at binding energy of 531.2 and 529.6 eV, indicating the coexistence of two types of surface oxygen species with different chemical environments. The former was assigned to be surface adsorption oxygen (O<sub>ads</sub>) species in a low-coordinated environment, whereas the latter was ascribed to surface lattice oxygen (O<sub>latt</sub>) in a coordinatively saturated environment. The variation in the relative intensity of the O<sub>ads</sub> and O<sub>latt</sub> signals suggested the change in the oxidation states of Mn during soot oxidation reaction. The O<sub>ads</sub>/O<sub>latt</sub> ratios of three samples were calculated and presented in Table 2. The O<sub>ads</sub>/O<sub>latt</sub> ratios followed the sequence of Mn<sub>3</sub>O<sub>4</sub>-HNS (0.59) > Mn<sub>3</sub>O<sub>4</sub>-ONS (0.42) > Mn<sub>3</sub>O<sub>4</sub>-NPS (0.39), which is in line with the orders of the surface Mn<sup>4+</sup> species. Obviously, the Mn<sub>3</sub>O<sub>4</sub>-HNS sample possessed the most surface adsorption oxygen species and the largest amount of oxygen vacancies, which could lead to the superior activity of (112) in Mn<sub>3</sub>O<sub>4</sub> hexagonal nanoplate particles than (101) facets for diesel soot oxidation.

The ratios of Mn<sup>4+</sup> and Mn<sup>2+</sup> species in three Mn<sub>3</sub>O<sub>4</sub> samples were all close 1:2 (Table 1), agreeing well with the possible oxide compositions of MnO<sub>2</sub>-2MnO. Furthermore, the exchange splitting energy of Mn 3 s ( $\Delta E_{3s}$ ) spectra was used to obtain more quantitative information about Mn valence ( $\nu_{Mn}$ ). Fig. 5C presented the Mn 3 s spectra of as-prepared Mn<sub>3</sub>O<sub>4</sub> with different shapes and all had unique bimodal structure at BE = 83.7 and 89.23 eV, which was caused by the coupling of the nonionized electron in the Mn 3 s orbital with the unpaired 3d

orbital electrons with parallel spins. According to the literature [42], the  $\Delta E_{3s}$  of Mn(II), Mn(III) and Mn(IV) was reported to 6.0, 5.4 and 4.5 eV, respectively. In this case, the observed  $\Delta E_{3s}$  for as-prepared Mn<sub>3</sub>O<sub>4</sub> samples were about 5.53 eV which was linearly related to  $\nu_{Mn}$ . Hence, the  $\nu_{Mn}$  were calculated by using the linear equation [43]:  $\nu_{Mn} = 9.67 - 1.27\Delta E_{3s} / \text{eV}$ . Based on the  $\Delta E_{3s}$  values (5.53 eV),  $\nu_{Mn}$  was calculated to be 2.65, which is in perfect match with the literature value of  $\nu_{Mn} = 2.66$  for Mn<sub>3</sub>O<sub>4</sub> materials [40]. This result was consistent with the previous reports about Mn<sub>3</sub>O<sub>4</sub> materials [44].

NO-TPSR and NO + O<sub>2</sub>-TPSR experiments were carried out to explore the interaction of probe molecules actually involved in soot combustion such as NO and O<sub>2</sub> with the catalyst surface. Fig. 6A clearly showed the different capability for NO<sub>2</sub> generation by surface active oxygen species over the samples, which was ranked as the decreased order of Mn<sub>3</sub>O<sub>4</sub>-HNS > Mn<sub>3</sub>O<sub>4</sub>-ONS > Mn<sub>3</sub>O<sub>4</sub>-NPS. It was evident that the Mn<sub>3</sub>O<sub>4</sub>-HNS sample with co-exposed (112) and (101) facets could afford the much more abundant surface reactive oxygen species for NO<sub>2</sub> generation than the other two samples with exposed (101) and (220) facets. The results were also consistent with the H<sub>2</sub>-TPR and XPS results.

The reactivities of Mn<sub>3</sub>O<sub>4</sub> samples with different shapes to oxidize NO were further examined by using NO + O<sub>2</sub>-TPSR. As seen from Fig. 6B, the formation signal of NO<sub>2</sub> ( $m/z = 46$ ) approached the thermodynamic equilibrium (NO + O<sub>2</sub> → NO<sub>2</sub>) with the rising temperature in the coexistence of gaseous 5000 ppm NO, 5 vol.% O<sub>2</sub> and balanced N<sub>2</sub>. The temperature to attain thermodynamic equilibrium of NO<sub>2</sub> oxidation followed the order of Mn<sub>3</sub>O<sub>4</sub>-HNS (346 °C) < Mn<sub>3</sub>O<sub>4</sub>-ONS (376 °C) < Mn<sub>3</sub>O<sub>4</sub>-NPS (424 °C). These results clearly demonstrated that the preferential exposure of (112) and (101) facets may favor NO oxidation capability of Mn<sub>3</sub>O<sub>4</sub> catalyst, which can be further correlated with the catalytic performance in terms of the NO<sub>2</sub>-assisted soot oxidation mechanism [5,8].

According to the literature [41], Mn cations with surface oxygen vacancies are the major active sites in facilitating the adsorption,

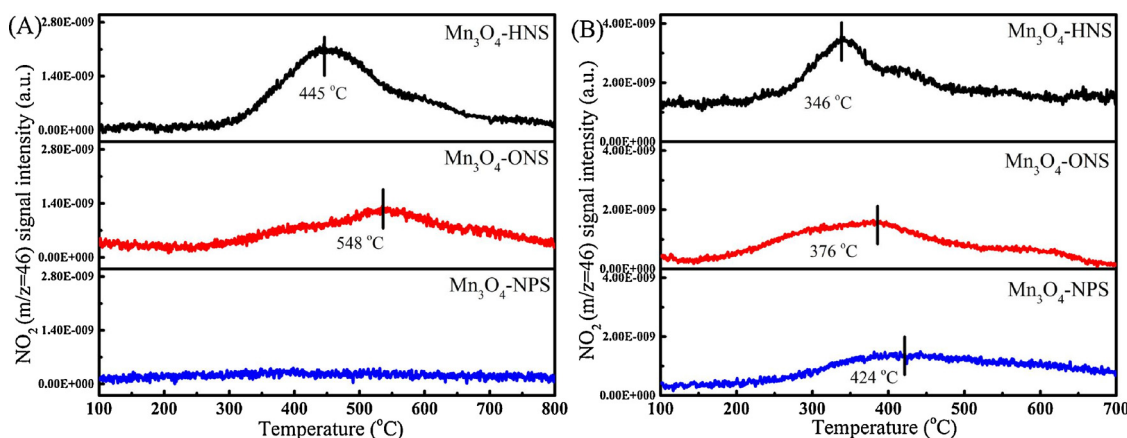


Fig. 6. NO-TPSR (A) and NO + O<sub>2</sub>-TPSR (B) curves for three Mn<sub>3</sub>O<sub>4</sub> samples (NO<sub>2</sub> (*m/z* = 46)).

activation and reaction of NO and O<sub>2</sub> molecules. Therefore, the Mn<sup>4+</sup> ions and adjacent oxygen vacancies (V<sub>O</sub>) are the major active sites in promoting NO oxidation. Hence, reaction mechanism of the NO<sub>2</sub> formed via NO oxidation reaction on Mn<sub>3</sub>O<sub>4</sub> catalyst can be rationalized by Langmuir-Hinshelwood mechanism in the coexistence of gaseous NO and O<sub>2</sub> (NO + O<sub>2</sub>-TPSR). Firstly, the Mn<sup>4+</sup> can adsorb NO to form the adsorbed nitric oxide (NO<sub>ads</sub>), which are further converted into a more active species NO<sup>+</sup> via electron transfer [39,45]. Meanwhile, the gaseous O<sub>2</sub> molecules could be dissociatively adsorbed and activated on the oxygen vacancies for generating active oxygen species. Secondly, such resultant NO<sup>+</sup> and surface active oxygen species can react with each other to yield a more powerful oxidant NO<sub>2</sub> than NO and O<sub>2</sub>, which can further boost soot combustion process via NO<sub>2</sub>-assisted mechanism.

Fig. 7 displayed the soot-TPR profiles of Mn<sub>3</sub>O<sub>4</sub>-HNS, Mn<sub>3</sub>O<sub>4</sub>-ONS, and Mn<sub>3</sub>O<sub>4</sub>-NPS catalysts. Soot-TPR illustrated that the soot particles could be oxidized by the surface reactive oxygen species existing on the catalysts under loose contact with Mn<sub>3</sub>O<sub>4</sub> powders in N<sub>2</sub> without gaseous oxygen. The soot/catalyst ratio before and after soot-TPR were determined to be 8.3 mmol/g<sub>cat</sub> and 5.8 mmol/g<sub>cat</sub>, respectively. Therefore, approximate 30% of the soot was burnt by the active oxygen species originated from the catalyst by checking the carbon balance of the soot-TPR analysis. With rising temperature from 200 °C to 800 °C, the CO<sub>2</sub>/CO concentrations can be identified in the soot-TPR profiles. The CO<sub>2</sub> was found to be the major product in the range of 0 ~ 0.3 vol.% whereas tracer amount of CO was detected in the range of 0 ~ 0.3 ppm.

The extremely low CO content in soot-TPR in this study is also in good agreement with the results reported by other research groups [4,46,47]. The CO<sub>2</sub> formed in high-temperature of 500–650 °C and 650–800 °C were attributed to the sub-surface lattice oxygen (denoted as  $\beta$ -O) and bulk lattice oxygen (denoted as  $\gamma$ -O), respectively, whereas the low-temperature range (250–500 °C) could be ascribed to the surface adsorbed oxygen species (denoted as  $\alpha$ -O, such as O<sup>−</sup> and O<sup>2−</sup>), which were active for catalytic oxidation [48]. In light of the temperature conditions in 200–600 °C for soot combustion, soot particles should be primarily oxidized by  $\alpha$ -O and  $\beta$ -O reactive oxygen species since  $\gamma$ -O with high reduction temperature exhibited poor reactivity with soot. Notably, the capability of the surface oxygen to oxidize soot over three samples followed the order of Mn<sub>3</sub>O<sub>4</sub>-HNS > Mn<sub>3</sub>O<sub>4</sub>-ONS > Mn<sub>3</sub>O<sub>4</sub>-NPS, in good agreement with the XPS and NO-TPSR results. The results provided valuable information of surface reactive oxygen species against soot. It is evident that the Mn<sub>3</sub>O<sub>4</sub>-HNS with (112) and (101) facets possessed the largest amount of surface adsorbed oxygen species ( $\alpha$ -O) as well as the active oxygen species among three samples. And the preferential exposure of (112) and (101) facets by proper tuning the shapes of the catalysts could lead to remarkably enhanced the amount of surface adsorbed oxygen to generate highly active oxygen species. Hence, it is anticipated that the Mn<sub>3</sub>O<sub>4</sub>-HNS exhibits the best catalytic activity for diesel soot combustion.

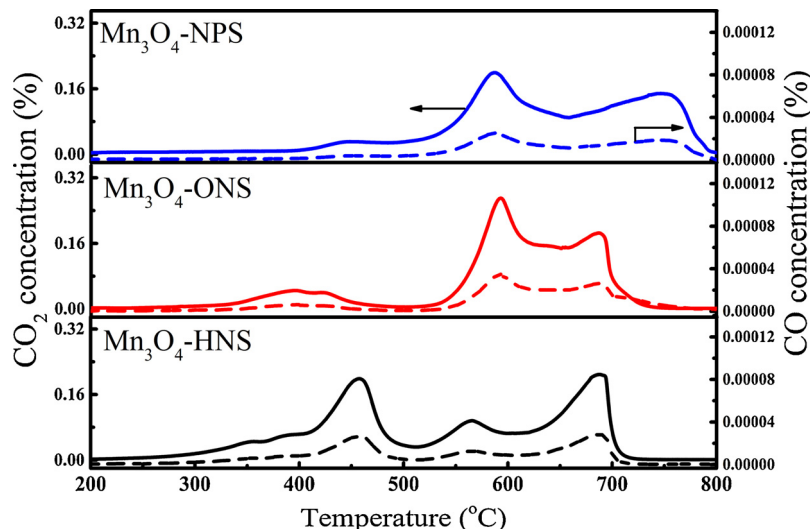


Fig. 7. Soot-TPR profiles for three Mn<sub>3</sub>O<sub>4</sub> samples (CO<sub>2</sub> (*m/z* = 44) and CO (*m/z* = 28)).

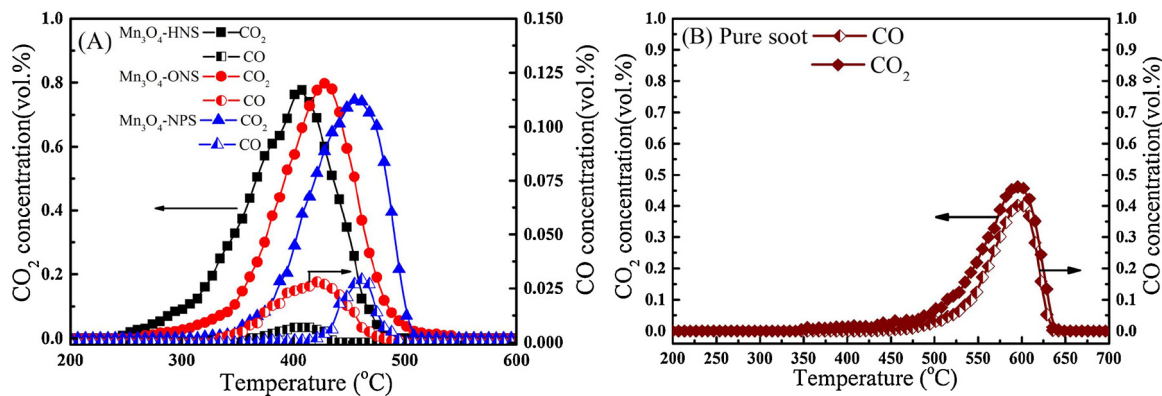


Fig. 8. Soot combustion performance for three  $\text{Mn}_3\text{O}_4$  samples on the same mass basis under loose contact mode (A) and pure soot (B) and the feed composition: 2500 ppm NO, 5 vol.%  $\text{O}_2$  and balanced by  $\text{N}_2$  with the total flow of 80 mL/min.

### 3.3. Catalytic performance of different $\text{Mn}_3\text{O}_4$ samples

The catalytic performance of diesel soot oxidation was evaluated using TPO method in the 2500 ppm NO and 5 vol%  $\text{O}_2$  atmosphere balanced by  $\text{N}_2$  under loose contact mode. As can be noted from Fig. 8, the ignition temperatures of all  $\text{Mn}_3\text{O}_4$  catalysts shifted to lower temperatures comparing with the ignition temperature of pure soot.  $T_m$  and  $S_{\text{CO}_2}^m$  were defined as the standard temperature and selectivity to compare the catalytic activity of all catalysts. The soot combustion activity under loose contact mode was ranked as the increasing order of pure soot <  $\text{Mn}_3\text{O}_4$ -NPS <  $\text{Mn}_3\text{O}_4$ -ONS <  $\text{Mn}_3\text{O}_4$ -HNS (Fig. 8A). It was obvious that the shapes of nanoscale  $\text{Mn}_3\text{O}_4$  had a significant impact on the catalytic combustion efficiency of soot and  $\text{Mn}_3\text{O}_4$ -HNS exhibited the highest activity for soot combustion with  $T_m$  of 407.7 °C and  $S_{\text{CO}_2}^m$  of 99.1%. The higher catalyst soot combustion activity for  $\text{Mn}_3\text{O}_4$ -HNS with co-exposed (112) and (101) crystal facets than  $\text{Mn}_3\text{O}_4$ -ONS with only (101) crystal facets can be closely related to the low-temperature reducibility and highly surface mobile oxygen species over the  $\text{Mn}_3\text{O}_4$ -HNS surface. The aforementioned results clearly implied the significant role of the active oxygen species on both (112) than (101) crystal facets towards soot combustion. In this sense, rational design and construction of special shapes and exposed crystal facets could be one of the effective strategies to boost soot combustion efficiencies.

Soot combustion is a typical gas-solid-solid three-phase heterogeneous catalytic reaction. Generally, the higher surface area of nanocatalyst was advantageous to increase the contact point between nanocatalyst and soot particles, which can subsequently enhance the catalytic soot oxidation activity by providing more active sites. In our work, the activity of soot combustion in Table 2 decreased as the order of  $\text{Mn}_3\text{O}_4$ -HNS >  $\text{Mn}_3\text{O}_4$ -ONS >  $\text{Mn}_3\text{O}_4$ -NPS, inconsistent with the order of the specific surface area of different  $\text{Mn}_3\text{O}_4$  samples, suggesting that chemical nature of the  $\text{Mn}_3\text{O}_4$  catalysts prevailed to be the crucial factor for overall reactivity. In order to further understand the effect of the shapes or exposed crystal facets over different  $\text{Mn}_3\text{O}_4$  samples on the difference in reactivity, kinetic study within the kinetic-relevant regime and the low soot conversion rates (below 12%) was carried out to derive the apparent activation energy ( $E_a$ ) values by using the Arrhenius equation where the specific reaction rate was normalized to per second and per unit specific surface area. As shown in Fig. 9 and Table 2, the  $E_a$  values increased in the sequence of  $\text{Mn}_3\text{O}_4$ -HNS with co-exposed (112) and (101) facets (56.4 kJ/mol) <  $\text{Mn}_3\text{O}_4$ -ONS with only (101) facets (86.4 kJ/mol) <  $\text{Mn}_3\text{O}_4$ -NPS with co-exposed (101) and (220) facets (100.6 kJ/mol), which is in reverse order of activity data obtained from the fixed bed reactor. The lower  $E_a$  values is, the easier the diesel soot can be catalytically burned. Our kinetic results can effectively rule out the effect of specific surface area. The specific reaction rates of the  $\text{Mn}_3\text{O}_4$  samples at 320 °C were calculated in Table 1. It is easy to find that the specially exposed crystal facet such as (112) and

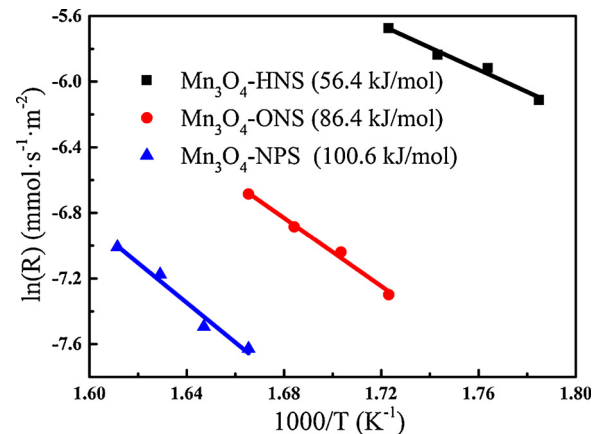


Fig. 9. Arrhenius-type plot of reaction rates for three samples.

(101) facets dramatically promote the soot combustion efficiency, suggesting that the essential role (112) facets for attaining superior reactivity on soot combustion. The above results were also well consistent with the XPS and  $\text{H}_2$ -TPR measurements.

Recent progress in experimental and computational catalysis has significantly improved our understanding of crystal facet-dependent reactivity changes in heterogeneous catalytic systems. A general consensus has been reached that the high-index planes of single-crystal surfaces generally often exhibit much higher catalytic activity than that of the most common stable planes [38]. Extensive experimental and theoretical studies have been devoted to understanding of diesel soot combustion over nano-scale metal oxide catalysts. Previous studies on nanocrystallite ceria with differently exposed crystal planes already implied that soot oxidation is structure sensitive on ceria [18]. More recently, we reported the soot combustion efficiency greatly depends on morphology and exposed crystal facet of  $\alpha\text{-Mn}_2\text{O}_3$ , and (001) facet with higher concentration of low-coordinated surface oxygen sites facilitates soot combustion process than (111) facets [17]. Ardizzone et al. [49] authenticated that the external surface of  $\text{Mn}_3\text{O}_4$  is  $2\text{MnO}\cdot\text{MnO}_2$  composition via XPS analyses for surface Mn species. Huang et al. [50] reported the  $\text{Mn}_3\text{O}_4$  hexagonal nanoplate with high miller-index (112) facets have a higher activity of than nanoparticles with (103) and (101) facets, and the structure dependence of catalytic oxidation of formaldehyde is explained by the different arrangement manner of surface atoms. Bogle et al. [51] pointed out that (112) facets show uncoordinated oxygen anions along the outer edges and the surface, resulting in higher intrinsic chemical reactivity than (101) or (110) planes via a study of the electrochemical impedance behaviors of orientation controlled  $\text{Mn}_3\text{O}_4$  nanocrystals. DFT calculations by Sun et al. show a structure selectivity for  $\text{O}_2$  adsorption, predicting the weak interaction

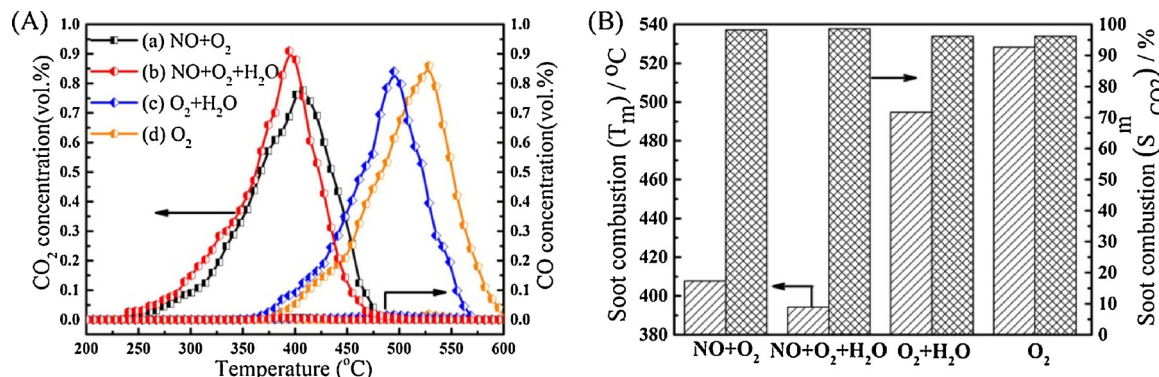


Fig. 10. The effect of feed compositions: the catalytic activity (A), T<sub>m</sub> and S<sub>CO2</sub><sup>m</sup> values (B) for soot combustion over Mn<sub>3</sub>O<sub>4</sub>-HNS sample under loose contact mode.

with oxygen for the coordination saturated (101) plane and strong interaction with O<sub>2</sub> on unsaturated coordinated on (001) facets containing high surface Mn valence [37]. In this work, hexagonal nanoplate with specially exposed (112) plane exhibited the best soot combustion efficiency on nanoscale Mn<sub>3</sub>O<sub>4</sub> with different shapes and crystal facets. The activity data can be satisfactorily explained by the measurements based on XPS, H<sub>2</sub>/soot-TPR and NO/NO + O<sub>2</sub>-TPSR. Our investigations point to the direction of improving the intrinsic catalytic activity of Mn<sub>3</sub>O<sub>4</sub> catalysts via modulating Mn<sub>3</sub>O<sub>4</sub> nanocrystals with more open surface structures e.g. (112) crystal facet in this case, which is also in good agreement with the literature reports.

### 3.4. Effect of contact mode

The contact mode between soot and catalyst as well as the number of contact points may have impact on the combustion efficiency of the soot oxidation process. The Mn<sub>3</sub>O<sub>4</sub> catalysts was evaluated under tight contact mode in the mixed gas of 2500 ppm NO, 5 vol.%O<sub>2</sub> and balanced N<sub>2</sub>. The experiment curves were shown in Fig. S5A and the T<sub>m</sub> values of all catalysts were reported in Fig. S5B. Notably, under the tight contact mode, the Mn<sub>3</sub>O<sub>4</sub> samples were ranked as the increased activity order of Mn<sub>3</sub>O<sub>4</sub>-NPS < Mn<sub>3</sub>O<sub>4</sub>-ONS < Mn<sub>3</sub>O<sub>4</sub>-HNS, in consistence with the loose contact mode. The catalytic activity of soot combustion over three Mn<sub>3</sub>O<sub>4</sub> samples in tight contact mode was superior to that in loose contact mode, similar to the previously reported results [10]. The results suggested the soot combustion efficiency of Mn<sub>3</sub>O<sub>4</sub> catalysts is sensitive to the contact mode, and tight contact mode may enlarge the contact between catalysts and soot. However, the tight contact mode can hardly serve as a standard protocol for the evaluation and screening of potential catalysts. This was because the contacting of soot and catalysts in tight contact mode is far away from the contact under the working condition in the tailpipe of diesel car. Working the catalyst/soot under loose contact mode would be more representative way to simulate the real contact of catalyst and soot. On the basis of the results, the catalytic activities of Mn<sub>3</sub>O<sub>4</sub> were affected by the contact mode, and the intimate contact between soot and catalyst leads to enhanced soot combustion efficiency.

In the absence of gaseous NO<sub>x</sub>, the difference in T<sub>m</sub> by varying soot-catalyst contact was often observed to be around 150 °C, as reported in the literatures [7,52]. However, the difference in T<sub>m</sub> by varying soot-catalyst contact can be dramatically reduced into the level of around 50–80 °C in the presence of NO<sub>x</sub>, as observed by us and also the authors in other groups [52–54]. Notably, the difference in the soot combustion due to the contact mode can not be completely eliminated in the presence of NO<sub>x</sub> under reaction conditions employed. The difference in the catalytic activity under tight and loose contact mode can be explained by the contribution of the overall combustion rate by different reaction pathways, i.e. the active oxygen species mechanism and NO<sub>x</sub>-assisted mechanism. The contribution of the active oxygen species mechanism

on the overall soot oxidation rate becomes much less significant under loose contact condition compared to that under tight contact mode, which explains why the same catalyst behaves less active under loose contact condition in the presence of NO. As shown in Fig. S6, NO plot shows the constant conversion/reaction trend despite the varying soot-catalyst contacts. The result is reasonable because we are using the same catalyst in both cases. It should be noted that NO content goes through the minimum at 350 °C, implying the attainment of the thermodynamic equilibrium of NO oxidation, which is also confirmed by our NO oxidation experiment in Fig. 6. NO oxidation is a gas-solid catalyzed reaction, which is independent on the contact mode of soot and catalyst.

### 3.5. Effects of NO and water vapor

In reality, soot and nitrogen oxide as the two primary contaminants are inevitably present in the diesel exhaust, and the actual effluent atmosphere of diesel exhaust always contains a certain quantity of water vapor. Therefore, Mn<sub>3</sub>O<sub>4</sub>-HNS sample with co-exposed (112) and (101) facets was chosen to investigate the effect of NO and water vapor on soot combustion. The influence of different feed compositions was investigated by using the same TPO procedure and the corresponding activity data were showed in Fig. 10. It was found that the T<sub>m</sub> and S<sub>CO2</sub><sup>m</sup> for Mn<sub>3</sub>O<sub>4</sub>-HNS were 528.3 °C and 96.2% in only O<sub>2</sub>, whereas the T<sub>m</sub> downshifted to lower temperature of 407.7 °C and S<sub>CO2</sub><sup>m</sup> increased to 98.2% in the presence NO. The similar experiment phenomenon was observed that the T<sub>m</sub> is downshifting from T<sub>m</sub> of 494.8 °C in the absence of NO to 394.3 °C in the presence of O<sub>2</sub>+H<sub>2</sub>O+NO (Fig. 10B). Thus, it was obvious that the NO existence should be particularly advantageous to enhance the catalytic soot combustion efficiency, which is fully in line with the “NO<sub>2</sub>-assisted” mechanism reported in the previous literatures [5,9,17,55]. It had been reported in the literatures that the soot combustion could be accelerated by catalytically promoting formation of NO<sub>2</sub> which is a much stronger oxidant than NO to boost soot combustion. Based on the above information, such NO<sub>2</sub>-assisted mechanism was also strongly dependent on the shapes and exposed facets of the Mn<sub>3</sub>O<sub>4</sub> samples. The results obtained from NO + O<sub>2</sub>-TPSR and NO-TPSR measurements over various Mn<sub>3</sub>O<sub>4</sub> could explain well why Mn<sub>3</sub>O<sub>4</sub>-HNS with co-exposed (112) and (101) facets had the better NO oxidation capability at low temperature. Hence, NO<sub>2</sub> formed via NO oxidation i.e. NO + 1/2O<sub>2</sub>→NO<sub>2</sub> played a crucial role during soot combustion reaction due to NO<sub>2</sub> participated actively in oxidizing soot into CO<sub>2</sub> or CO and completed the catalysis cycle during the soot combustion (i.e. 2NO<sub>2</sub>+C→CO<sub>2</sub>+NO) [56]. The investigation of NO oxidation reactivity over catalyst materials may serve as a very useful shortcut for the preliminary screening of the potential catalysts.

Combining activity data and characterization results (NO + O<sub>2</sub>-TPSR, HR-TEM, H<sub>2</sub>-TPR and XPS results), it is clear that the preferential exposure of (112) and (101) facets may favor NO oxidation capability

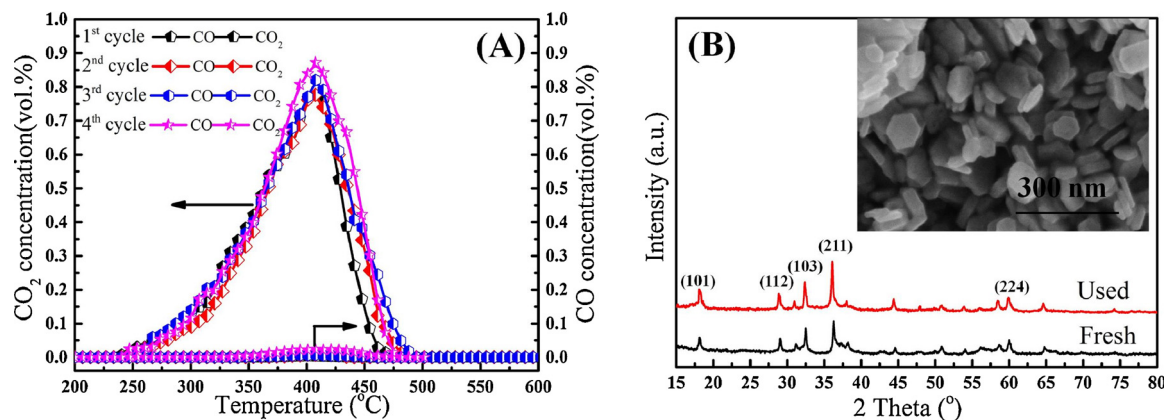


**Fig. 11.** The stability test of Mn<sub>3</sub>O<sub>4</sub>-HNS sample under loose contact mode, the feed composition: 2500 ppm NO, 5 vol.% O<sub>2</sub> and balanced by N<sub>2</sub> with the total flow of 80 mL/min.

over Mn<sub>3</sub>O<sub>4</sub> catalyst with abundant surface Mn<sup>4+</sup> and active oxygen species, which can be further correlated with the catalytic performance of soot combustion in terms of the NO<sub>2</sub>-assisted soot oxidation mechanism.

The influence of 10 vol.% water vapor on the soot combustion was investigated over Mn<sub>3</sub>O<sub>4</sub>-HNS under two kinds of conditions 2500 ppm NO + 5 vol.% O<sub>2</sub> and 5 vol.% O<sub>2</sub>, N<sub>2</sub> as balance gas. The activity data curves were shown in Fig. 10A(b and c). The T<sub>m</sub> and S<sub>CO2</sub><sup>m</sup> were 407.7 °C and 98.2% in the feed gases with NO + O<sub>2</sub> while the T<sub>m</sub> value decreased by 13.4 °C and S<sub>CO2</sub><sup>m</sup> increased slightly in the presence of H<sub>2</sub>O (Fig. 10B). Comparing soot combustion efficiency in O<sub>2</sub> and O<sub>2</sub> + H<sub>2</sub>O, it was clear that the T<sub>m</sub> values downshifted significantly towards lower temperatures, decreasing from 528.3 °C to 494.8 °C in the presence of H<sub>2</sub>O. The water vapor and NO showed positive impact on the catalytic soot combustion efficiency. In addition, it is hypothesized that the major role of water vapor for soot oxidation was to enhance the NO<sub>2</sub>-assisted soot oxidation reactivity by boosting oxidation of NO into NO<sub>2</sub> production. Based on the previous reports [39,57], in the existence of NO and H<sub>2</sub>O vapor, the OH radicals generated from O atoms and H<sub>2</sub>O molecules facilitate the re-oxidation of the metal oxide vacancies by the consumption of oxygen. Moreover, a DFT study by Chen et al. [39] also showed that 14 wt.% moisture may promote NO<sub>2</sub> molecules desorption from the active sites and facilitate NO adsorption on the refreshed surface active sites. Therefore, H<sub>2</sub>O vapor may play an important role in promoting the soot oxidation via NO<sub>2</sub>-assisted soot oxidation mechanism, as evidenced by Fig. 10A in this study and many others' work [5,47,53].

Our previous work and the results from other groups [5,17,57,58] have evidenced that the water vapor could boost the soot combustion efficiency with different explanations. The results in this work also clearly showed the feed gas containing 10 vol% H<sub>2</sub>O vapor had a positive effect on improving the soot combustion efficiency regardless of the presence of NO. It was suggested that the positive effect of H<sub>2</sub>O might be ascribed to the wetting role, just like that of alkali metal (such as K, Na), which improved the contact between soot and catalyst in the absence of NO, thus boosting the soot combustion efficiency. Also the 10 vol.% H<sub>2</sub>O vapor might possibly act as a reactant in soot oxidation and generate intermediates (such as hydroxyl radicals, oxygen-containing complexes) on soot-catalyst contact surface with utilization of O<sub>2</sub> and NO, thus favoring the enhancement of the soot combustion activity. Uchisawa et al. [58] proposed that H<sub>2</sub>O vapor played a promotion role in hydrolysis and decarboxylation of the highly stable carbon surface species formed from partial oxidation of the reacting carbon surface via NO<sub>2</sub>-attack in the soot elimination process.

### 3.6. The catalytic stability of Mn<sub>3</sub>O<sub>4</sub>-HNS sample

The stability of the best-performing Mn<sub>3</sub>O<sub>4</sub>-HNS sample with hexagonal nanoplate shape was investigated by recycling tests under loose contact condition. As shown in Fig. 11A, the T<sub>m</sub> and S<sub>CO2</sub><sup>m</sup> retained almost unchanged after four times of recycling tests, indicating the strong stability against deactivation. The outstanding durability of Mn<sub>3</sub>O<sub>4</sub>-HNS could be attributed to the highly stables crystal phase and shape. Fig. 11B showed the nearly same XRD pattern after the four times of recycling experiments. Furthermore, the FE-SEM inset in Fig. 11B illustrated that after soot-TPO cycles the Mn<sub>3</sub>O<sub>4</sub>-HNS sample remained their original hexagonal nanoplate shape. Our results demonstrated the promising potential of using Mn<sub>3</sub>O<sub>4</sub>-HNS as catalyst candidate for the soot combustion.

The hydrothermal stability was investigated on Mn<sub>3</sub>O<sub>4</sub>-HNS with well-defined hexagonal nanoplate morphology after being aged in water vapor for 4 h at 850 °C. It can be observed from Fig. S7, the Mn<sub>3</sub>O<sub>4</sub>-HNS after aging treatment show the almost the same catalytic activity for soot combustion compared with the Mn<sub>3</sub>O<sub>4</sub>-HNS. Meanwhile, Fig. S7B shows almost the same XRD diffraction peaks on the used Mn<sub>3</sub>O<sub>4</sub>-HNS catalysts as the fresh one. These results suggest that the Mn<sub>3</sub>O<sub>4</sub>-HNS catalyst own excellent thermal stability.

## 4. Conclusions

In this study, we have successfully synthesized three nanostructure Mn<sub>3</sub>O<sub>4</sub> catalysts with different shapes (hexagonal nanoplate, octahedral, and nanoparticles) by facile methods. The Mn<sub>3</sub>O<sub>4</sub>-HNS with hexagonal nanoplate shape exhibited superior catalytic soot combustion performance with respect to the octahedral Mn<sub>3</sub>O<sub>4</sub>-ONS and Mn<sub>3</sub>O<sub>4</sub>-NPS samples. The present results indicated that this facet-dependent reactivity of Mn<sub>3</sub>O<sub>4</sub> nanocrystal was originated from the chemical nature of the co-exposed (112) and (101) facets. As revealed by H<sub>2</sub>-TPR, XPS, NO-TPSR, soot-TPR, and NO + O<sub>2</sub>-TPSR, the superior activity of Mn<sub>3</sub>O<sub>4</sub>-HNS sample can be well correlated with its enhanced low-temperature reducibility, abundant surface Mn<sup>4+</sup> species and surface reactive oxygen species, and the high NO oxidation activity, which were rooted from its increased fraction of exposed (112) facets. Moreover, the effect of feed composition investigated in loose contact mode illustrated that NO and H<sub>2</sub>O was indispensable in promoting soot combustion efficiencies. Furthermore, Mn<sub>3</sub>O<sub>4</sub>-HNS displayed both excellent structural and activity stability after 4 runs of recycling tests and aging treatment, demonstrating its promising potential as low cost and eco-friendly catalysts for highly effective practical soot combustion.

## Acknowledgements

This work is supported by the Program for Professor of Special Appointment (Eastern Scholar) at Shanghai Institutions of Higher Learning, the Talent Program of Shanghai University of Engineering Science, National Natural Science Foundation of China (21503133), Shanghai Automotive Industry Science and Technology Development Foundation (1721), Science and Technology Commission of Shanghai Municipality (18030501100), Shanghai Talent Development Foundation (2017076), Municipal Education of Shanghai (ZZGCD15031), the Education Ministry Key Lab of Resource Chemistry of Shanghai (2016No.3), Innovation Fund for Graduate Students (17KY0404), Zhanchi Plan (nhrc-2015-12), Task-based Knowledge Innovation Team (2014td16) and Startup Foundation (2015-20) of Shanghai University of Engineering Science.

## Appendix A. Supplementary data

Supplementary material related to this article can be found, in the online version, at doi:<https://doi.org/10.1016/j.apcatb.2018.09.092>.

## References

- [1] M. Cortés-Reyes, C. Herrera, M.Á. Larrubia, L.J. Alemany, *Appl. Catal. B Environ.* 193 (2016) 110–120.
- [2] R. Kimura, J. Wakabayashi, S.P. Elangovan, M. Ogura, T. Okubo, *J. Am. Chem. Soc.* 130 (2008) 12844–12845.
- [3] Y. Yu, J. Ren, D. Liu, M. Meng, *ACS Catal.* 4 (2014) 934–941.
- [4] C. Cao, L. Xing, Y. Yang, Y. Tian, T. Ding, J. Zhang, T. Hu, L. Zheng, X. Li, *Appl. Catal. B Environ.* 218 (2017) 32–45.
- [5] J.M. Christensen, J.-D. Grunwaldt, A.D. Jensen, *Appl. Catal. B Environ.* 205 (2017) 182–188.
- [6] G. Yang, Y. Li, Y. Men, *Catal. Commun.* 69 (2015) 202–206.
- [7] M. Piumetti, S. Bensaid, N. Russo, D. Fino, *Appl. Catal. B Environ.* 165 (2015) 742–751.
- [8] T. Andana, M. Piumetti, S. Bensaid, L. Veyre, C. Thieuleux, N. Russo, D. Fino, E.A. Quadrelli, R. Pirone, *Appl. Catal. B Environ.* 209 (2017) 295–310.
- [9] N.D. Wasalathantri, T.M. SantaMaria, D.A. Kriz, S.L. Dissanayake, C.-H. Kuo, S. Biswas, S.L. Suib, *Appl. Catal. B Environ.* 201 (2017) 543–551.
- [10] Z. Shang, M. Sun, S. Chang, X. Che, X. Cao, L. Wang, Y. Guo, W. Zhan, Y. Guo, G. Lu, *Appl. Catal. B Environ.* 209 (2017) 33–44.
- [11] X. Lin, S. Li, H. He, Z. Wu, J. Wu, L. Chen, D. Ye, M. Fu, *Appl. Catal. B Environ.* (2017).
- [12] Y. Wei, J. Liu, Z. Zhao, Y. Chen, C. Xu, A. Duan, G. Jiang, H. He, *Angew. Chem. Int. Ed. Engl.* 50 (2011) 2326–2329.
- [13] J. Wang, L. Cheng, W. An, J. Xu, Y. Men, *Catal. Sci. Technol.* 6 (2016) 7342–7350.
- [14] J. Wang, G. Yang, L. Cheng, E.W. Shin, Y. Men, *Catal. Sci. Technol.* 5 (2015) 4594–4601.
- [15] Y.-F. Sun, J.-H. Li, Y.-Q. Zhang, B. Hua, J.-L. Luo, *ACS Catal.* 6 (2016) 2710–2714.
- [16] C. Lee, Y. Jeon, S. Hata, J.-I. Park, R. Akiyoshi, H. Saito, Y. Teraoka, Y.-G. Shul, H. Einaga, *Appl. Catal. B Environ.* 191 (2016) 157–164.
- [17] L. Cheng, Y. Men, J. Wang, H. Wang, W. An, Y. Wang, Z. Duan, J. Liu, *Appl. Catal. B Environ.* 204 (2017) 374–384.
- [18] E. Aneggi, D. Wiater, C. de Leitenburg, J. Llorca, A. Trovarelli, *ACS Catal.* 4 (2014) 172–181.
- [19] G. Zhai, J. Wang, Z. Chen, W. An, Y. Men, *Chem. Eng. J.* 337 (2018) 488–498.
- [20] Y. Wei, Z. Zhao, J. Liu, S. Liu, C. Xu, A. Duan, G. Jiang, *J. Catal.* 317 (2014) 62–74.
- [21] S.K. Megarajan, S. Rayalu, M. Nishibori, Y. Teraoka, N. Labhsetwar, *ACS Catal.* 5 (2015) 301–309.
- [22] T. Andana, M. Piumetti, S. Bensaid, L. Veyre, C. Thieuleux, N. Russo, D. Fino, E.A. Quadrelli, R. Pirone, *Appl. Catal. B Environ.* 226 (2018) 147–161.
- [23] Y. Li, W. Shen, *Chem. Soc. Rev.* 43 (2014) 1543–1574.
- [24] F. Fang, N. Feng, L. Wang, J. Meng, G. Liu, P. Zhao, P. Gao, J. Ding, H. Wan, G. Guan, *Appl. Catal. B Environ.* 236 (2018) 184–194.
- [25] T. Liu, Q. Li, Y. Xin, Z. Zhang, X. Tang, L. Zheng, P.-X. Gao, *Appl. Catal. B Environ.* 232 (2018) 108–116.
- [26] S.C. Kim, W.G. Shim, *Appl. Catal. B Environ.* 98 (2010) 180–185.
- [27] B. Bai, J. Li, J. Hao, *Appl. Catal. B Environ.* 164 (2015) 241–250.
- [28] J. Duan, S. Chen, S. Dai, S.Z. Qiao, *Adv. Funct. Mater.* 24 (2014) 2072–2078.
- [29] E. Saputra, S. Muhammad, H. Sun, H.-M. Ang, M.O. Tadé, S. Wang, *Appl. Catal. B Environ.* 154–155 (2014) 246–251.
- [30] P. Zhang, Y. Zhan, B. Cai, C. Hao, J. Wang, C. Liu, Z. Meng, Z. Yin, Q. Chen, *Nano Res.* 3 (2010) 235–243.
- [31] J. Mondal, P. Borah, S. Sreejith, K.T. Nguyen, X. Han, X. Ma, Y. Zhao, *ChemCatChem* 6 (2014) 3518–3529.
- [32] Z.Y. Fei, B. Sun, L. Zhao, W.J. Ji, C.T. Au, *CHEM.* 19 (2013) 6480–6487.
- [33] T.R. Bastami, M.H. Entezari, *Chem. Eng. J.* 164 (2010) 261–266.
- [34] J. Zhao, J. Nan, Z. Zhao, N. Li, J. Liu, F. Cui, *Appl. Catal. B Environ.* 202 (2017) 509–517.
- [35] Y. Li, H. Tan, X.Y. Yang, B. Goris, J. Verbeeck, S. Bals, P. Colson, R. Cloots, G. Van Tendeloo, B.L. Su, *Small* 7 (2011) 475–483.
- [36] S.Z. Huang, J. Jin, Y. Cai, Y. Li, H.Y. Tan, H.E. Wang, G. Van Tendeloo, B.L. Su, *Nanoscale* 6 (2014) 6819–6827.
- [37] J. Liu, L. Jiang, T. Zhang, J. Jin, L. Yuan, G. Sun, *Electrochim. Acta* 205 (2016) 38–44.
- [38] N. Tian, Z.Y. Zhou, S.G. Sun, Y. Ding, Z.L. Wang, *Science* 316 (2007) 732–735.
- [39] J. Wang, J. Zhu, X. Zhou, Y. Du, W. Huang, J. Liu, W. Zhang, J. Shi, H. Chen, *J. Mater. Chem. A Mater. Energy Sustain.* 3 (2015) 7631–7638.
- [40] A. Ramírez, P. Hillebrand, D. Stellmach, M.M. May, P. Bogdanoff, S. Fiechter, *The J. Phys. Chem. C* 118 (2014) 14073–14081.
- [41] F. Liu, H. He, Y. Ding, C. Zhang, *Appl. Catal. B Environ.* 93 (2009) 194–204.
- [42] V.R. Galakhov, M. Demeter, S. Bartkowski, M. Neumann, N.A. Ovechkina, E.Z. Kurmaev, N.I. Lobachevskaya, Y.M. Mukovskii, J. Mitchell, D.L. Ederer, *Phys. Rev. B* 65 (2002) 113102.
- [43] E. Beyreuther, S. Grafström, L.M. Eng, C. Thiele, K. Dörr, *Phys. Rev. B* 73 (2006) 155425.
- [44] Z. Geng, Y. Wang, J. Liu, G. Li, L. Li, K. Huang, L. Yuan, S. Feng, *ACS Appl. Mater. Interfaces* 8 (2016) 27825–27831.
- [45] Z. Shu, Y. Chen, W. Huang, X. Cui, L. Zhang, H. Chen, G. Zhang, X. Fan, Y. Wang, G. Tao, D. He, J. Shi, *Appl. Catal. B Environ.* 140–141 (2013) 42–50.
- [46] N. Guilhaume, B. Bassou, G. Bergeret, D. Bianchi, F. Bosselet, A. Desmartin-Chomel, B. Jouquet, C. Mirodatos, *Appl. Catal. B Environ.* 119–120 (2012) 287–296.
- [47] B.R. Stanmore, J.F. Brillhart, P. Gilot, *Carbon* 39 (2001) 2247–2268.
- [48] Q. Li, M. Meng, N. Tsubaki, X. Li, Z. Li, Y. Xie, T. Hu, J. Zhang, *Appl. Catal. B Environ.* 91 (2009) 406–415.
- [49] S. Ardizzone, C.L. Bianchi, D. Tirelli, *Colloids Surf. A Physicochem. Eng. Asp.* 134 (1998) 305–312.
- [50] K.A.M. Ahmed, Q. Zeng, K. Wu, K. Huang, *J. Solid State Chem.* 183 (2010) 744–751.
- [51] J. Liu, Y.H. Ng, M.B. Okatan, R. Amal, K.A. Bogle, V. Nagarajan, *Electrochim. Acta* 130 (2014) 810–817.
- [52] W. Kaspera, P. Indyka, Z. Sojka, A. Kotarba, *Catal. Sci. Technol.* 8 (2018) 3183–3192.
- [53] H. Zhang, S. Yuan, J. Wang, M. Gong, Y. Chen, *Chem. Eng. J.* 327 (2017) 1066–1076.
- [54] D. Fino, N. Russo, G. Saracco, V. Specchia, *J. Catal.* 242 (2006) 38–47.
- [55] V. Alcalde-Santiago, A. Davó-Quíñonero, D. Lozano-Castelló, A. Bueno-López, *Appl. Catal. B Environ.* 234 (2018) 187–197.
- [56] W. Wang, M. Geoffrey, K. Neeti, G. Yuan, B. Shan, M. Nguyen, M.G. Uschi, H.D. Burtron, J. Gary, C. Kyeongjae, X. (Kelly) Hao, *Science* (80-) 337 (2012) 832–835.
- [57] H. Ranji-Burachaloo, S. Masoomi-Godarzi, A.A. Khodadadi, Y. Mortazavi, *Appl. Catal. B Environ.* 182 (2016) 74–84.
- [58] J. Oi-Uchisawa, A. Obuchi, A. Ogata, R. Enomoto, S. Kushiyama, *Appl. Catal. B Environ.* 21 (1999) 9–17.